Minerals Engineering 204 (2023) 108413

Contents lists available at ScienceDirect

Minerals Engineering

journal homepage: www.elsevier.com/locate/mineng

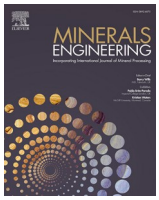

Synthesis of Cu-Al layered double hydroxides from aluminum saline slags

A.I. Boulahbal [a], L. Santamaría [a], A. Azizi [b], M. Boutahala [c], S.A. Korili [a], A. Gil [a,*]

[a] INAMAT, Science Department, Los Acebos Building, Public University of Navarra, Campus of Arrosadia, E-31006 Pamplona, Spain
[b] Laboratory of Chemistry, Molecular Engineering and Nanostructures, Chemistry Department, Universityof Ferhat Abbas Setif-1, 19000 Setif, Algeria
[c] Laboratory of Chemical Process Engineering, Department of Process Engineering, Faculty of Technology, University of Ferhat Abbas Setif-1, 19000 Setif, Algeria

ARTICLE INFO

Keywords:
Layered double hydroxides
Hydrotalcite
Copper
Jahn-Teller effect
Aluminum saline slag
Industrial waste

ABSTRACT

The use of saline slag, a hazardous waste generated during the recycling of aluminum, as aluminum source for the synthesis CuAl layered double hydroxides (LDH) is for the first time reported in this study. Due to the Jahn-Teller effect, divalent copper–aluminum LDH come usually with impurities and a pure CuAl LDH is not easy to obtain. The effect of synthesis pH has been examined by comparing LDH synthesized at various pH, ranging from 6 to 12 via a co-precipitation method using aluminum obtained from an alkaline extraction of the slag. For comparison purposes, a sample was synthesized at pH = 9 using commercial aluminum $Al(NO_3)_3{\cdot}9H_2O$ instead of extracted aluminum. The effects of the aging time and calcination temperature are also discussed. The LDH and their calcined metal mixed oxide (layered double oxide, LDO) have been analyzed with several characterization techniques: powder X-ray diffraction (PXRD), N_2 adsorption at −196 °C, thermogravimetric analysis (TGA), temperature programmed reduction (TPR), scanning electron microscopy (SEM), transmission electron microscopy and energy-dispersive X-ray spectroscopy (TEM and EDS). Synthesis pH has been proved not only to have a significant effect on the nature of secondary phases but also on the structure and morphology of the samples.

1. Introduction

A significant amount of aluminum dross is produced each year during aluminum smelting, generating quantities of between 15 and 25 kg of aluminum dross per 100 kg of molten aluminum (Mahinroosta and Allahverdi, 2018; Gao et al., 2021). Saline slag is the main waste generated during secondary aluminum processes (Tenorio and Espinosa, 2002). It is considered a hazardous waste, given its composition and its possible reaction with water.

Aluminum can be almost completely recycled into new products, unlike other metals, by smelting processes using tilting rotary kilns and a mixture of salts (brine) such as NaCl and KCl. These play crucial roles in this process, especially by allowing the transfer of heat to the metal and preventing its oxidation. They are also used to dissolve, absorb and allow metal oxides and other impurities to be easily separated from metallic aluminum (Tenorio and Espinosa, 2002). Saline slag consists of metallic aluminum and flux brines as main components, but also several oxides can be found in the composition. The percentage equivalent to these oxides in the form of non-metallic products (NMP) varies according to the nature of the recycled material (Verma et al., 2020; Gil, 2005; Gil and Korili, 2016; Gil et al., 2014). The management of saline slag may require separation of its constituents for eventual recycling and application, or storage, which requires controlled landfills. It should be noted that the aluminum present in the saline slag can be recovered as a high-valuable product by either acid or basic leaching, in order to be used for the preparation of several functional materials, including hexaaluminates (Torrez-Herrera et al., 2022), zeolites (Yoldi et al., 2020); layered double hydroxides (Santamaría et al., 2020; Gil et al., 2018) and pillared clays (Cardona et al., 2021). Several studies rely on acid leaching to perform the extractions, however the synthesis of LDH must be carried out at a basic pH, which implies a basic extraction of the aluminum (Gil et al., 2018).

Layered double hydroxides (LDH) also called hydrotalcite compounds are two-dimensional (2D) inorganic nanomaterials with the molecular formula $[M(II)_{1-x}M(III)_x(OH)_2]^{x+}(A^{n-})_{x/n}{\cdot}mH_2O$, wherein M^{II} and M^{III} are exemplary divalent (Mg^{2+}, Ni^{2+}, Co^{2+}, Zn^{2+}, Cu^{2+}, etc.) and trivalent metal ions (Al^{3+}, Cr^{3+}, Fe^{3+}, V^{3+}, Ga^{3+}, etc.), respectively. A^{n-} is the interlayer anion which could be CO_3^{2-}, Cl^-, NO_3^-, SO_4^{2-}, amon others (Bukhtiyarova, 2019; Nejati et al., 2018) (see Fig. 1). Moreover, x expresses the molar ratio $x = M^{III}/(M^{II} + M^{III})$ whose value is between 0.2 and 0.33 for the pure LDH phase (Obalová et al., 2009). They are made up of positively charged brucite-like ($Mg(OH)_2$) layers where the

* Corresponding author.
E-mail address: andoni@unavarra.es (A. Gil).

https://doi.org/10.1016/j.mineng.2023.108413
Received 27 March 2023; Received in revised form 6 August 2023; Accepted 23 September 2023
Available online 29 September 2023

cations are octahedrally coordinated with OH − and in which the trivalent cations partially replace the divalent ones. An interlayer region containing charge compensating exchangeable anions and solvation molecules also exist in the interlamellar region (Nejati et al., 2018). These functional materials are considered an emerging and versatile class of synthetic layered anionic clays that have received much attention in various environmental fields where LDH serve as photocatalysts and adsorbents (Guo et al., 2011; Guan et al., 2022; Lu et al., 2016). They can also be employed in catalysis (Fan et al., 2014), separation processes (Arabi et al., 2016; Asfaram et al., 2017), nanotechnology (Mohammadnezhad et al., 2015) and as supports (Hubbell and Chilkoti, 2012) among other significant uses. They are highly effective due to their extraordinary physico-chemical properties as well as their excellent anion exchange capacity, specific surface area, chemical resistance, ease of synthesis, adaptable structure (Sanvicens and Marco, 2008; Dinari et al., 2017) as well as their good redox behaviour (Nagendra et al., 2015; Zhang et al., 2014). The copper-containing hydrotalcite represents a particular system in this family of compounds, having an electronic configuration of Cu^{2+}, that causes a deformation of the structure of the octahedra $Cu(OH)_2$ due to the Jahn-Teller effect (Cudennec and Lecerf, 2001) thus making the preparation of LDH precursors containing only copper as M^{2+} difficult. Great efforts have been made to produce binary copper/aluminum hydrotalcites (Yamaoka et al., 1989; Lwin et al., 2001; Valente et al., 2000; Segal et al., 2003), although frequently other phases such as malachite, gibbsite or copper oxide are found hence disclosing the difficulty of the synthesis process. In order to avoid them, another metal is usually added forming a ternary system (Cu^{2+} M^{2+} M^{3+}). Several metals have been tried such as (Co^{2+}, Mg^{2+}, Ni^{2+}, Zn $^{2+}$) as M^{2+} or (Al^{3+}, Cr^{3+}, Fe^{3+} Ce^{3+}, Ga^{3+}) as M^{3+} (Montanari et al., 1997; Xia et al., 2015; Li et al., 2018; Yadav et al., 2022). These LDH or their derived oxides have been tested for various purposes, especially as catalysts and catalyst supports (Fornari et al., 2017; Bart and Sneeden, 1987; Dib et al., 2020; Kannan, 2006; van Everbroeck et al., 2022; Shannon et al., 1996; Busetto et al., 1984; Velu and Swamy, 1996) thanks to the interesting catalytic performance of copper ions.

Keeping in mind the growing interest for LDH in recent years and although many types of hydrotalcites have been synthesized, the innovative option chosen in this work is to develop functional materials of layered double hydroxides type containing pure phase Cu from aluminum saline slag residues as a source of aluminum which, to our knowledge, has not been explored so far (Santamaría et al., 2022). We have studied the characterization of LDH as well as calcined mixed metal oxides (LDO) with various physical and chemical techniques in order to better understand their structure–property relationship. The synthesis and characterization of CuAl LDH hydrotalcite prepared at various pH values with a fixed molar ratio M^{2+}/M^{3+}=3 by the coprecipitation method and using an aqueous solution of Na $_2CO_3$ as the precipitant is reported in this work.

2. Experimental procedure

2.1. Materials

The synthesis of hydrotalcites was performed using $Cu(NO_3)_2{\cdot}3H_2O$ (Labkem, ≥ 98%), and Na_2CO_3 (Sigma-Aldrich, ≥ 99.99%). HNO_3 was used for pH adjustment and NaOH (Panreac) for both pH adjustment and aluminum extraction (see next section). $Al(NO_3)_3{\cdot}9H_2O$ (Acros Organics, ≥ 99.99%) was used for the synthesis of the commercial aluminum sample.

2.2. Synthesis of compounds of the hydrotalcite type LDH and its mixed metallic oxide, LDO

The aluminum was obtained from the saline slag by an alkaline extraction process: 5 g of the slag were added to 100 mL of a 2 mol/L NaOH solution, it was placed in a stirred reflux system at 500 rpm for 1 h and at a temperature of 100 °C. Centrifugation was used to separate the suspension, the aluminum present in the centrifuged solution was found to be 9.6 (±) 0.14 g/L (0.35 mol/L), determined by ICP-OES. Besides

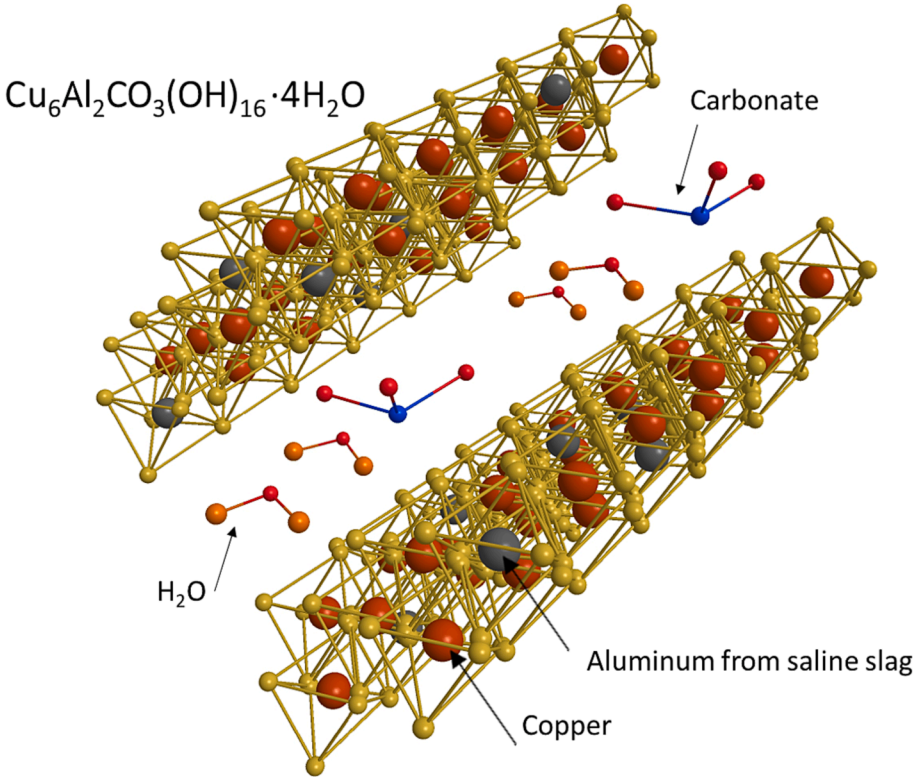

Fig. 1. Model structure of CuAl LDH.

aluminum, small amounts of other metals such as silicon, copper, potassium, and iron, among others, have also been extracted (see Table 1).

LDH were synthesized by the co-precipitation method, with a molar ratio of Cu/Al: M^{2+}/M^{3+}=3:1. Seven samples were synthesized with the same ratio and changing the pH value in a range from 6 to 12. As an example, 0.3 mol/L of copper II nitrate trihydrate ($Cu(NO_3)_2{\cdot}3H_2O$) and the aluminum from the extraction, slightly diluted (0.1 mol/L) were added dropwise to a 0.1 mol/L Na_2CO_3 solution. The synthesis pH was adjusted to 8 using both NaOH and HNO_3 as required. The mixture was stirred at 700 rpm and 60 °C until finishing to add the two solutions and then left to age for 24 h. Milli-Q water was used to wash the samples and they were then centrifuged (8000 rpm, 5 min) as many times as necessary until the pH was lowered to 7. All materials were dried at 80 °C for 16 h and manually grinded with pestle in a mortar. The samples were denoted by their synthesis pH as CA6, CA7, CA8, CA9, CA10, CA11 and CA12 for pH = 6,7,8,9,10,11 and 12, respectively. For LDO, a certain amount of each LDH sample was calcined at 400 °C for 2 h and named CCA8, CCA9, CCA10 and CCA11. For comparison purposes, a sample was synthesized at pH = 9 using commercial aluminum $Al(NO_3)_3{\cdot}9H_2O$ instead of extracted aluminum, named CA9X and CCA9X (when calcined at 400 °C).

2.3. Characterization techniques

X-ray powder diffraction (PXRD) patterns were recorded on a D8 ADVANCE ECO BRUKER instrument using Ni-filtered Cu Kα radiation (λ = 0.15418 nm) in a 2θ range of 5 at 70° and 2° (2θ)/min scan rate. The working current of the X-ray source was 25 mA and the voltage was 40 kV. The Eva software and Xpert Hightscore Plus were used for the identification of the crystalline phases present in the samples which were carried out by comparison with the JCPDS diffraction files (ICDD database). The size of the crystallites was determined from the experimental diffractograms using the Debye-Scherrer equation. The textural properties of the solids were analyzed using a Micromeritics ASAP 2020 Plus adsorption analyzer by adsorption of N_2 at − 196 °C. Before the adsorption measurements, the samples (0.2 g) were degassed at 200 °C and pressures below 0.133 Pa for 4 h. BET specific surface area (S_{BET}) was calculated from adsorption data obtained over the relative pressure range of 0.05–0.20. The thermogravimetric (TG) measurements were recorded in a METTLER TOLEDO model TGA/DSC 3 + brand device. The samples were heated from 40 to 700 °C with a heating rate of 20 °C/min under an atmosphere of N_2 (50 mL/min). Temperature programmed reduction (TPR) studies were performed on a Micromeritics TPR/TPD 2900 instrument under a flow rate of 30 mL/min and a 5% concentration of H_2 in Ar (Praxair) to reduce the samples from room temperature to 1000 °C. Finally, the morphological analysis and the chemical composition of the samples were carried out by SEM (INSPECT F50, Mode: 30 kV - Map, Detector: BSED) and TEM images were obtained with a coupled CCD camera (Gatan) in a Tecnai F30 microscope (Thermofisher) at a working voltage of 300 KV. Spatial resolution in this microscope in TEM mode is 0.15 nm. Also, in order to analyze the chemical composition of the materials, X-ray Energy Dispersive Spectra (EDS) were obtained with an EDAX detector.

3. Results and discussion

3.1. Structural properties

X-ray powder diffraction patterns of uncalcined and calcined samples are visible in Figs. 2 and 3. First, a study was conducted on the effect of pH on the formation of the hydrotalcite phase for CuAl LDH, followed by the effect of the rest time and the calcination temperature. pH has an important impact on the formation of the layered structure in LDH, the relevance of pH throughout the synthesis is illustrated in Fig. 2 **A, B**. The synthesis of CuAl LDH was carried out by changing the pH parameter within a range of 6 to 12, while other parameters were fixed (3/1 Cu/Al molar ratio, synthesis temperature 60 °C, aging time 24 h at room temperature). According to the results included in Fig. 2**-A** LDH prepared in a range of pH between 6 and 11, exhibits CuAl reflections corresponding to the layered double hydroxide structure. For the case of sample CA6 there are reflections at 11.9, 23.5 and 35.5°, which

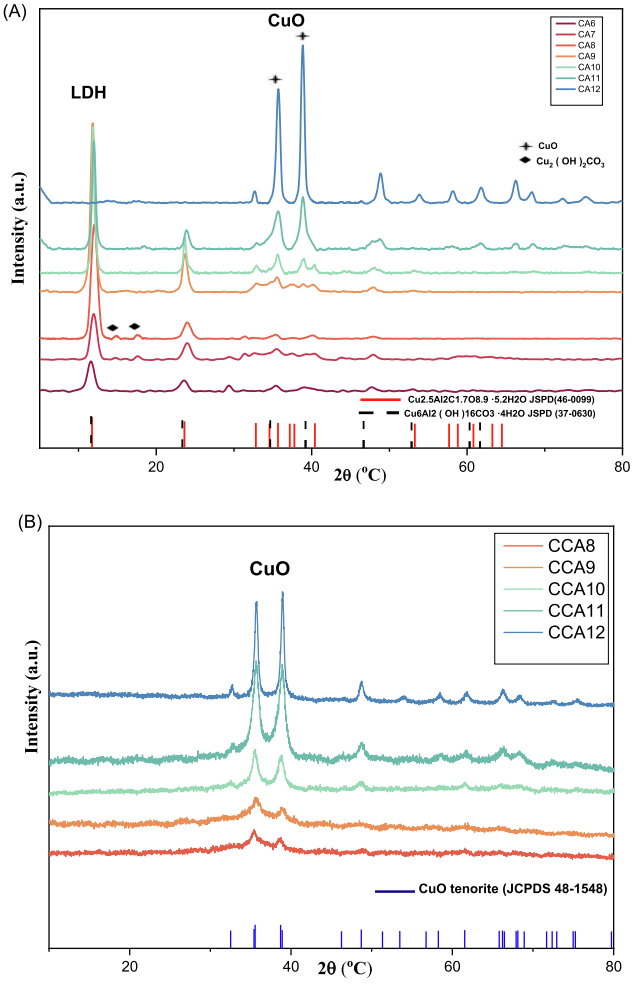

Fig. 2. Powder X-Ray diffraction diagrams (PXRD). **(A)** Effect of the synthesis pH on the LDH. pH = 6,7,8,9,10,11 and 12 correspond to CA6, CA7, CA8, CA9, CA10, CA11 and CA12 samples. The crystal patterns of copper oxide (JCPDS 48-1548) and copper hydroxide carbonate (JSPD 01-072-0075) correspond to, respectively. Monoclinic copper Aluminum Carbonate Hydroxide Hydrate, red bands (JCPDS 46-0099) and rhombohedral, black bands (JCPDS 37-0630). **(B)** LDO and pH ranging from 8 to 12, corresponding to CCA8, CCA9, CCA10, CCA11 and CCA12. Crystal patterns of copper oxide tenorite in blue lines (JCPDS 48-1548). (For interpretation of the references to colour in this figure legend, the reader is referred to the web version of this article.)

Table 1
Chemical composition of the solution after basic extraction by ICP-OES.

Element	Al	Na	Si	Cu	Fe	K	Ca	Mg	Ni
Composition (g/L)	9.60	41.83	0.16	0.0019	0.0016	0.0067	0.08	<0.02	<0.03

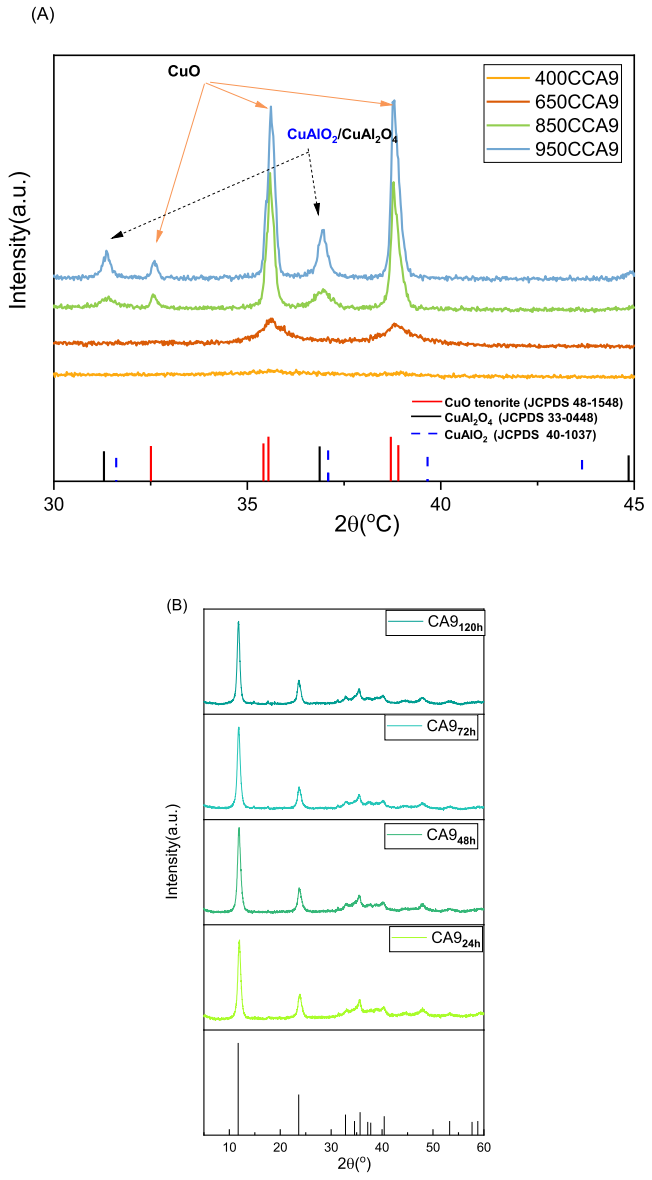

Fig. 3. Powder X-ray diffraction (PXRD) patterns. (A) LDO at various calcination temperatures. 400CCA9, 650CCA9, 850CCA9, 950CCA9 for temperatures 400, 650, 850 and 950 °C, respectively. CuO tenorite (solid red lines ((JCPDS 48-1548)), $CuAl_2O_4$ (solid black lines (JCPDS 33-0448) and $CuAlO_2$ (solid blue lines (JCPDS 40-1037)). (B) LDH precursor by rest time effect from 24 to 120 h corresponding to CA924h, CA948h, CA972h and CA9120h. Copper Aluminum Carbonate Hydroxide Hydrate monoclinic (solid black lines (JCPDS 46-0099). (For interpretation of the references to colour in this figure legend, the reader is referred to the web version of this article.)

correspond to the diffractions of planes (003), (006) and (012) respectively, also corresponding to the model reported for a sample $Cu_6Al_2(OH)_{16}CO_3{\cdot}4H_2O$ (JSPD 037–0603). Thus, highlighting the formation of a layered double hydroxide structure with R-3 m rhombohedral symmetry similar to those found by several other authors (Fan et al., 2014; Tien Thao and Kim Huyen, 2015; Angelescu et al., 2008). In the case of samples CA7 and CA8, it can be seen the formation of more crystalline hydrotalcites with a slight displacement, which may be due to a transition of the structure from rhombohedral to monoclinic. The reflections which appear at 14.93, 17.60, 31.23° are identified as an additional impurity phase of malachite (JSPD 01–072-0075). It is well known that this type of hydrotalcites is always mixed with this phase as impurities due to the Jahn-Teller effect at the Cu^{2+} ion level (Lwin et al., 2001; Valente et al., 2000; Segal et al., 2003). Maintaining the pH of the synthesis at 9 makes it possible to obtain a hydrotalcite with higher purity, while at pH = 10 the diffraction line appearing at 39.07° is identified as copper oxide. Another difference between these samples is in the intensity of the reflections. As the pH increases, the intensity of the reflections grows and the linewidth decreases, which corresponds to an increase in crystallinity. A further increase in precipitation pH leads to the formation of more crystalline copper oxides as can be seen for the sample CA11. This may be due to the rapid oxidation of copper, and the formation of a more soluble $Al(OH)_4^-$ instead of $Al(OH)_3$ (Sertsova et al., 2015) (the presence of the latter being important for carrying out the formation of a laminar double hydroxide type compound (Boclair and Braterman, 1999) followed by a decrease in crystallinity due to the incorporation of Cu^{2+} cations within the layer. All reflections observed in these last three samples were indexed to the monoclinic unit cell using the cell parameters given by *Yamaoka et al.* (Yamaoka et al., 1989) (a = 1.521 nm, b = 0.29 nm, c = 0.586 nm, β = 100,3°) (JSPD 046–0099). This structure takes into account the deformation of the $Cu(OH)_2$ octahedron by the Jahn-Teller effect in the structure. These results are consistent with data reported by other authors (Li et al., 2015; Britto and Vishnu Kamath, 2009). The CA12 sample shows a different structure from those of the previous samples, with the precipitation of a predominant CuO crystalline phase and no sign of hydrotalcites since at strong alkaline pH, the hydrotalcite phase being a copper-hydroxy complex becomes more soluble and therefore dissolves in solution following solubility curves and predominance diagrams for Cu^{2+} (Haraketi et al., 2017). This sample was not considered for further characterization. CuAl LDH is the most stable at pH = 9, at higher or lower pH the cations Al^{3+} and Cu^{2+} remain partially in the supernatant solution and the precipitation is incomplete, i.e. the precipitated quantities of aluminum and copper vary according to the OH^- ions in accordance with *Yamaoka et al.* (Yamaoka et al., 1989). It is concluded that the pH has a significant impact on the formation of LDH and this by its effect on the precipitation of cations: the more the pH increases, the more important the content of precipitated copper is which is demonstrated by the results of EDS (see Table 2). Hence, the Jahn-Teller effect leads to a lowering of symmetry followed by a formation of a monoclinic cell. Therefore, a gradual transition from the rhombohedral structure to the monoclinic structure can be observed as the copper content increases, which in accord to the work reported by *Intissar et al.* (Intissar et al., 2015).

The X-ray powder diffraction patterns comparison of the two samples synthesized at a pH of 9, using commercial Al on one side (CA9X) and extracted Al on the other (CA9), shows that in sample CA9X the formation of a layered double hydroxide structure with monoclinic symmetry is similar to that found in sample CA9. The difference lies in the sample synthesized with $Al(NO_3)_3$, where well-defined peaks with an increase in peak intensities can be seen, indicating higher crystallinity in this solid **(Fig. S1-A).** Moreover, it is important to emphasize the existence of peaks between 53° and 65°, which are absent in sample CA9.

It is well known that calcination can increase the adsorption capacity of LDH by producing LDO (Berner et al., 2018). The XRD patterns for LDO (CuAl oxides) obtained by calcining CuAl LDH at 400 °C for 2 h are included in Fig. 2**-B**. XRD peaks for all CuAl oxides were assigned to CuO (JCPDS 48–1548). No other phase was detected. The crystal phases of copper in the calcined LDO material also depend on the pH parameter, in materials where the pH is higher the diffraction patterns show finer and better-defined peaks and, consequently, greater crystallinity. In the case of the CCA9X sample, peaks are more defined than that of the sample synthesized by aluminum extraction **(Fig. S1-B)** and the formation of CuO can be clearly observed.

The effect of the temperature of calcination can be seen in Fig. 3**-A** and **Fig. S2.** The intensity and sharpness of XRD reflections in LDO calcined at temperatures above 650 °C (i.e. 850 and 950 °C) is significantly greater than those below with the appearance of new peaks identified as $CuAl_2O_4$ spinel and $CuAlO_2$ thus indicating the destruction

Table 2
Structural and textural features of the CuAl LDH samples.

Samples	Phase	Atomic [a] (%)		Cu/Al	dp[b] (nm) LDH	dp[b] (nm) CuO	dp[c] (nm) LDH	S_{BET} (m^2/g) uncalcined	S_{BET} (m^2/g) calcined
		Cu	**Al**						
CA6	LDH very low	60.35	29.58	2.04	7.6	0	*	30	*
CA7	LDH low	54.03	24.77	2.18	8.4	0	*	46	*
CA8	LDH medium	65.27	30.57	2.13	8.79	0	10.25	48	46
CA9	LDH high	70.56	27.31	2.58	10.69	0	*	60	55
CA10	LDH, CuO low	70.56	28.71	2.45	16.42	10.84	16.09	50	26
CA11	LDH low, CuO medium	74.95	23.29	3.21	14.16	10.26	15.25	56	29
CA12	CuO	*	*	*	0	17.46	*	52	*

a: Obtained via EDS analysis, b: HDL crystallite size determined by the Debye–Scherrer equation based on (2 0 0) peak and CuO crystallite size based on (1 1 1) peak, c: Obtained via TEM análisis, * not determined.

of LDH. The crystalline peaks corresponding to the phase of Al_2O_3 were not detected indicating that it exists in either semi-crystalline or amorphous form (Song et al., 2013). The aging time was also considered as one of the parameters controlling crystallinity and particle size. This variable was studied by synthesizing the different CuAl LDH samples and changing the aging time while other parameters were fixed (3/1 Cu/Al molar ratio, synthesis pH maintained at 9 and 60 °C). XRD patterns of samples prepared, dried at room temperature and aged for 24, 48, 72 and 120 h, respectively, are shown in Fig. 3**-B**. As the synthesis time increases, all the precipitates show a pattern similar to hydrotalcite with a uniform growth of reflections. The X-ray diffraction peaks of the precipitate with a synthesis time of 24 h fully correspond to the layered structure, while at 120 h, more intense peaks indicate a higher degree of crystallinity of the samples. The crystallinity of the hydrotalcites increased with increasing aging time (Sertsova et al., 2015; Haraketi et al., 2017).

3.2. Textural properties

The morphologies and microstructures of LDH materials synthesized with a molar ratio of 3:1 at the same conditions of temperature and agitation but with the variation of the concentrations of [OH^-] ions in the solution (pH = 8, 10, 11) were characterized by SEM and TEM images. The SEM images of CA8, CA10 and CA11, respectively, shown in Fig. 4 (**A1, B1, C1**) allow to visually observe the morphology of the characteristic platelet-like material with disorderly packing typical of hydrotalcites (Li et al., 2015; Song et al., 2013; High et al., 2022; Aflak et al., 2022; Kühl et al., 2012), in concordance to XRD results. A series of TEM images at several scales and resolutions for hydrotalcite samples are included in Fig. 4 **(A2-5, B2-5, C2-5)**. In the case of CA8, (Fig. 4A1-5), we observe two types of well-defined structures where amorphous agglomerated blocks (dp_{Avrg} = 144 nm) and platelet laminar structures with (dp_{Averg} = 10 nm) are found. These values calculated by TEM correspond to those found in the DRX diffractograms (dp_{Averg} = 8.79 nm,

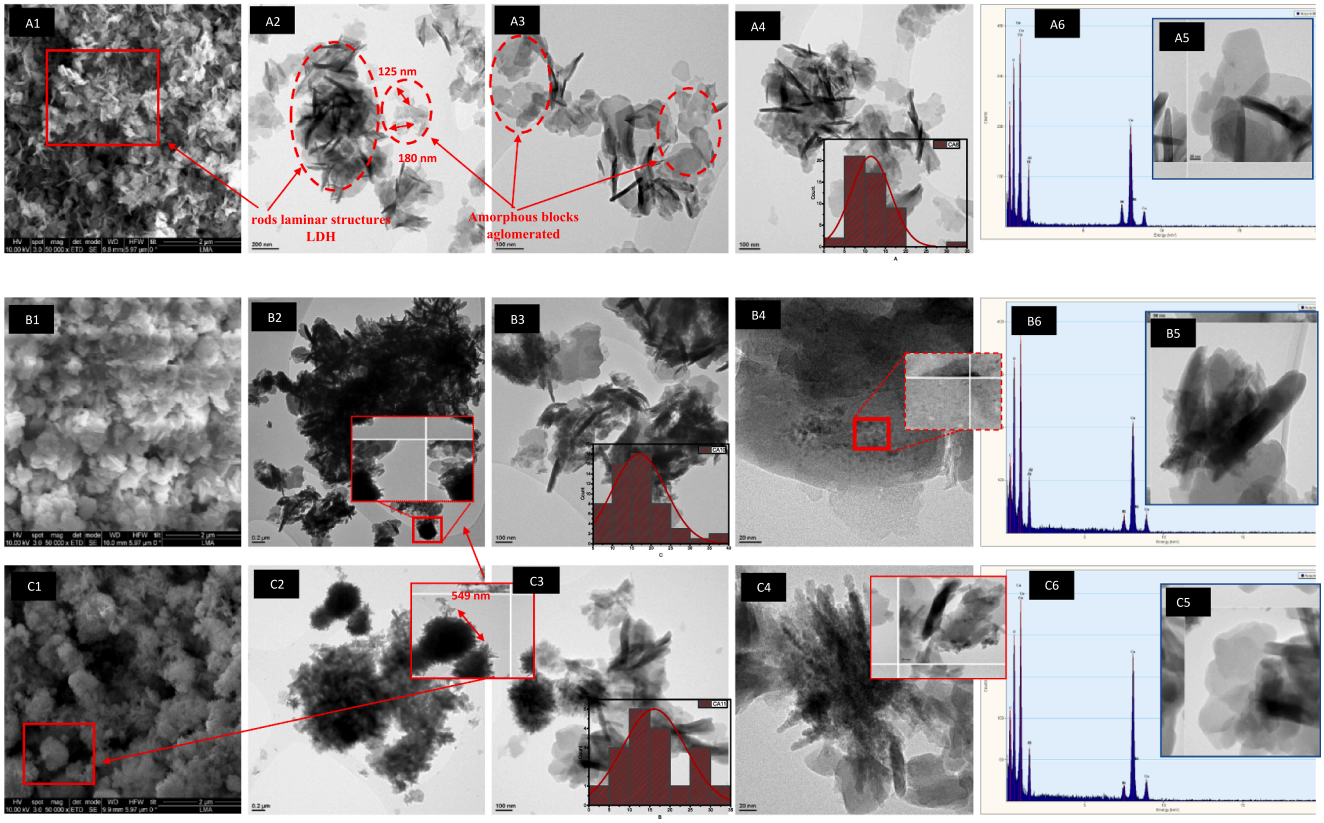

Fig. 4. SEM/TEM images of CuAl LDH prepared from co-precipitation at various pH. **(A1-B-C1)** SEM of CA8-CA10-CA11 samples with pH = 8–10-11, respectively. **(A2-5, B2-5, C2-5)** STEM micrographs at different scales for CA8-CA10 and CA11, respectively. **(A6-B6-C6)** EDX micrographs for CA8-CA10-CA11.

see Table 2), attributed to CuAl LDH. The amorphous blocks in this sample could be attributed to a secondary phase of malachite identified in the diffractograms of Fig. 2**A**. In CA8 the density of lamellar structures per μm^2 in the sample is practically by the same as that of amorphous blocks. For the CA10 sample (Fig. 4B1-5), in addition to finding the structures of amorphous blocks and lamellar structures, a new formation of agglomerates of rosette-shaped nanospheres is present (zoom Fig. 4 **B2**) which could be attributed to CuO nanoparticles which by action of the new charge balance Al^{+3}-Cu^{+2}/$[OH^{-}]$/$[CO_3]^{-2}$ adopts this morphology and generates these structures. In CA10 sample, a substantial increase in LDH laminar structures can be observed compared to both the amorphous structures and the agglomerates of copper oxide nanoparticles. The laminar structures in CA10 have a bigger size, around 16 nm (see Table 2) and with a much higher density than that of sample CA8. The presence of metallic Cu nanoparticles is also observed from zoom Fig. 4 **B4**. In the case of the last CA11 sample, here the predominant morphology is that of spherical rosettes of agglomerated crystals which may belong to clusters of oxide-type copper (dp = 500 nm, Fig. 4 **C2**), notably reducing the laminar structures and large amorphous blocks. These indicate that with the logarithmic increase of OH^- ions, the amphoteric $Cu(OH)_2$ becomes more soluble which causes a decomposition of LDH and favors the precipitation of CuO hence the appearance of the latter and the decrease of the former, highlighting what was observed in the DRX models. This phenomenon can also be explained indicating that the increase in OH^- ions generates repellent effects of aluminum forms, favoring a selective interaction with copper and the appearance of these CuO structures. The EDX (Fig. 4 **A6-B6-C6**) patterns determined for the samples show concentrations of aluminum, copper and nickel. The nature of the metallic Al solution extracted from aluminum entails the presence of traces of other metals such as Si, Fe, Na already identified through ICP analysis (see Table 1) which, due to the sensitivity of the EDX technique, are not detected. The histogram of the size distribution of CuAl LDH without calcination obtained by determining the diameters between 25 and 50 nanoparticles is included in Fig. 4 (**A4-B3-C3**, bottom right). The mean diameter was determined at 10.25, 16.09 and 15.25 nm for CA8, CA10 and CA11, respectively.

A comparison of the calcined (CCA8-CCA9-CCA10) and non-calcined (CA8-CA10-CA11) samples is presented in Fig. 5 where it can be seen that the increase in pH, as previously stated, generates a greater amount of CuO in surface for calcined samples and dispersed Cu nanoparticles in non-calcined samples. In the case of pH = 8 (CA8 and CCA8) (Fig. 5A7-9), the TEM image once the sample has been calcined (see image A8 and zoom A8) shows the appearance of a large amount of spherical 3D copper oxide particles that have grown on the surface. In the SEM (**A7**) images, it can be observed the spherical agglomerates of these nanoparticles which have grown on the LDH structures, due to the surface diffusion effect and the sintering reaction activated by the calcination temperature. If we compare these samples with the uncalcined samples (Fig. 4 **A1**), only platelet/rod type laminar microstructures are visible, since Cu is dispersed on the material. In the sample at pH = 10, the same behavior as the previous one is observed, where the CuO particles that have grown on the LDH surface generate the blocking of the surface of the LDH, covering practically all the material (see Fig. 5 **B8** and zoom B8), thus generating a significant decrease in the specific surface area (see Table 2), which makes it impossible to detect structures by XRD. Regarding the sample at pH = 11, both in the calcined (CCA11) and non-calcined (CA11) samples, copper oxide structures with rosette-like morphologies and 3D spherical agglomerates can be found, that end up blocking and trapping in the calcined sample the few LDH structures present (Fig. 5**C8**). Image D (HRTEM) confirmed copper oxide crystals with a lattice spacing of 0.25 nm.

All nitrogen adsorption/desorption isotherms at −196 °C of CuAl LDH/LDO as seen in Fig. 6 (**6-A** for uncalcined samples and **6-B** for calcined samples), show similar profiles belonging to type IV having a hysteresis loop of type H3 according to the IUPAC classification, indicating a mesoporous structure and narrow plate-like particles (Dib et al., 2020; Brunauer et al., 1940; Palapa et al., 2020). A more detailed definition of the hysteresis loops is also included in **Fig. S3.** It is possible to partly attribute the increase in S_{BET} to structural transformations of the LDH, increasing crystallite size with increasing pH as the driving gradient (see Table 2). As crystallite size increases in the synthesis process the surface increases and the LDH phase is enriched up to pH = 9 (see Fig. 7). This effect could be related to the increase in both the interlaminar spaces and the quantity of these structures with increasing pH, as observed in TEM images. At pH = 10 (CA10), the appearance of the secondary CuO phase was observed with a crystallite size of 10.84 nm (determined by XRD) and 16.42 nm for LDH. The S_{BET} is maintained up to a pH = 12 and it is observed that the S_{BET} of the samples CA11 (pH = 11) is dominated by the NP of CuO agglomerated in spherical structures of the 3D rosette type which make it possible to obtain a value of (55 m^2/g) with interstices and different textural properties. As can be seen, the pH variation, under the aforementioned conditions, directly affects the type of structures to be obtained, the quantity, the enrichment and the type of secondary phases, as well as the morphological and textural properties of the synthesized samples (see Fig. 7), making it possible to obtain the structural evolution as a function of the electrochemical potential and/or the concentration of the OH^- ions. It should be mentioned that the final values of the specific surface area of the calcined samples, for high Cu/Al molar ratios, generate relatively low values due to excess Cu and phase competition. If the specific surface observed for CA9 is compared with CA9X, the use of extracted aluminum produces a slight increase of 50 to 60 m^2/g. This increase can be related to a greater porosity produced by the presence of other metals in solution. (see Table 1).

The thermogravimetric analysis derived from the hydrotalcite-type samples were carried out in a nitrogen atmosphere. The TG curves as well as the corresponding derived TG curves (DTG) representative for the uncalcined samples are shown in Fig. 8. All precipitates containing hydrotalcite-like phases were found to exhibit similar TG and DTG curves. Significant weight loss occurs primarily in four stages, begins at room temperature and ends around 700 °C. As can be seen from the results included in Table 3, the existence of these stages explains the difference in mass loss between the samples. According to previously reported data (Haraketi et al., 2017; Kannan et al., 2004; Voyer et al., 2009), the TG diagram showed that the first corresponding weight loss of approximately 3% occurring below 160 °C is due to the loss of water from the surface of the materials and physisorbed gas. The following step spreads up to 210 °C accounts for about 9–10% mass loss for samples at pH = 8–9 and 6–5% for pH = 10–11, respectively, corresponds to the elimination of water molecules from the interlayer. The third stage, shows the total loss of the intercalated water, the de-nitration, the dehydroxylation as well as the beginning of the decomposition of the interlaminar carbonate anions in the form of CO_2. At this stage a fraction of metal oxides is formed. Large mass loss is recorded for sample CA8 probably due to decomposition of malachite producing simultaneously H_2O and CO_2 which is proved by DTG signal at around 325 °C (Bridier et al., 2010), absent in the other samples. It can be noted that the solids at pH lower than 11, having a greater amount of LDH structure, obtained the greatest loss of mass in zones II and III, as also noted in the CCA9X sample **(Fig. S4)** with a total weight loss of 27% **(Table S1).** This can be related to the large capacity of water adsorption of aluminum hydroxide and to the structural change from LDH to copper oxide that appeared in sample CA10. The last step which occurred at high temperatures (above 570 and up to 700 °C) showed an abrupt mass loss for all materials, due to the decarbonation phase. The main losses are visible on the DTG diagrams of Fig. 8: the corresponding curves show three endothermic signals which follow one another, the first peak located around 180 °C corresponds to the dehydration of the intercalated water, the second at around 260 °C is due to the dehydroxylation of the brucite-type layers the last is from to the decomposition of the more stable carbonate anion (Song et al., 2013).

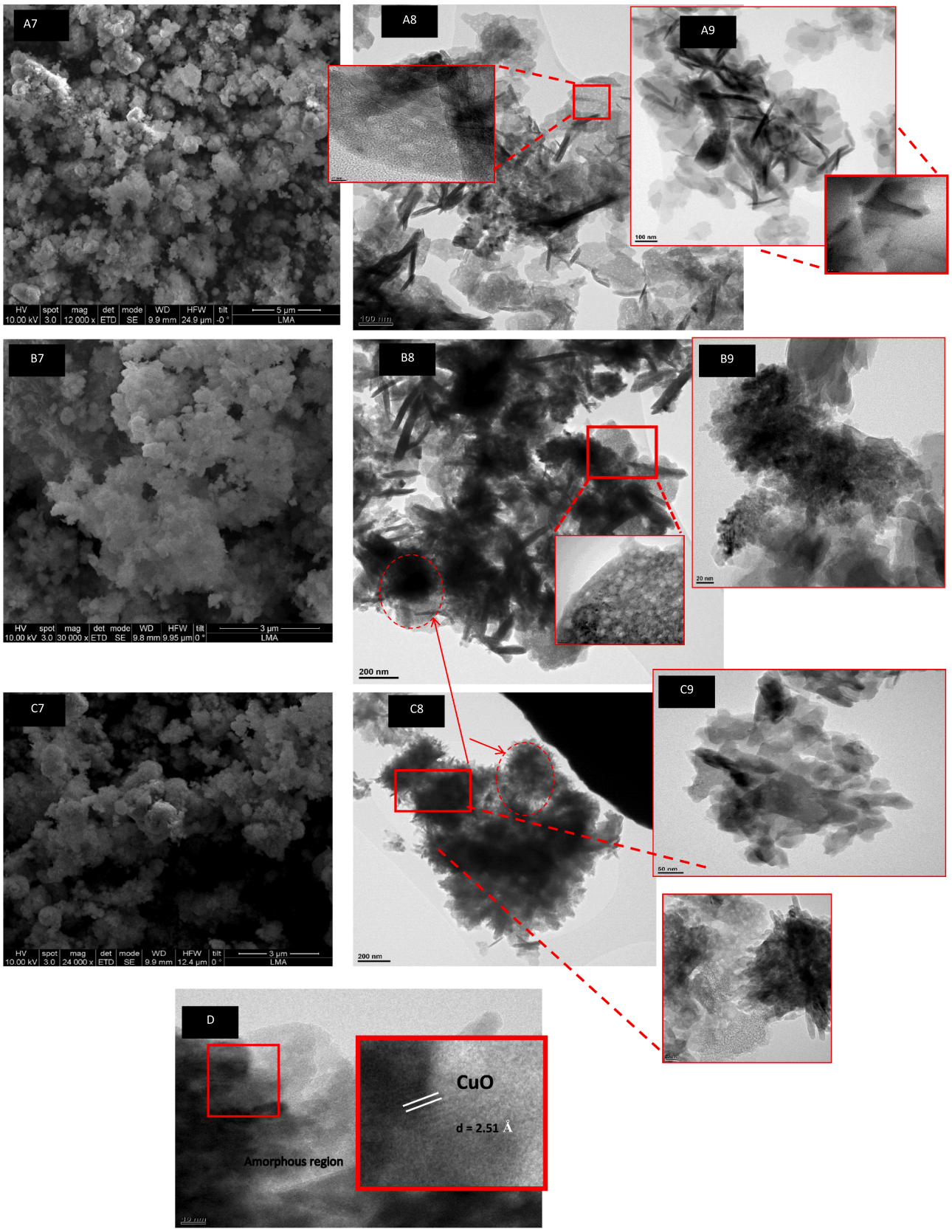

Fig. 5. SEM and comparison of images TEM for calcined and uncalcined samples. **(A7-B7-C7)** SEM of CCA8-CCA10-CCA11, calcined samples. **(A8-B8-C8)** STEM micrographs of CCA8-CCA10-CCA11, calcined samples. **(A9-B9-C9)** STEM micrographs of the CuAl LDH precursor prepared from co-precipitation method at various pH. **(D)** HRTEM image of mixed metal oxides calcined at 400 °C and pH = 10 The lattice edges with a separation of 0.251 nm, is in according to the XRD interplanar d spacing (0.252 nm) of monoclinic tenorite CuO (JCPDS 48-1548).

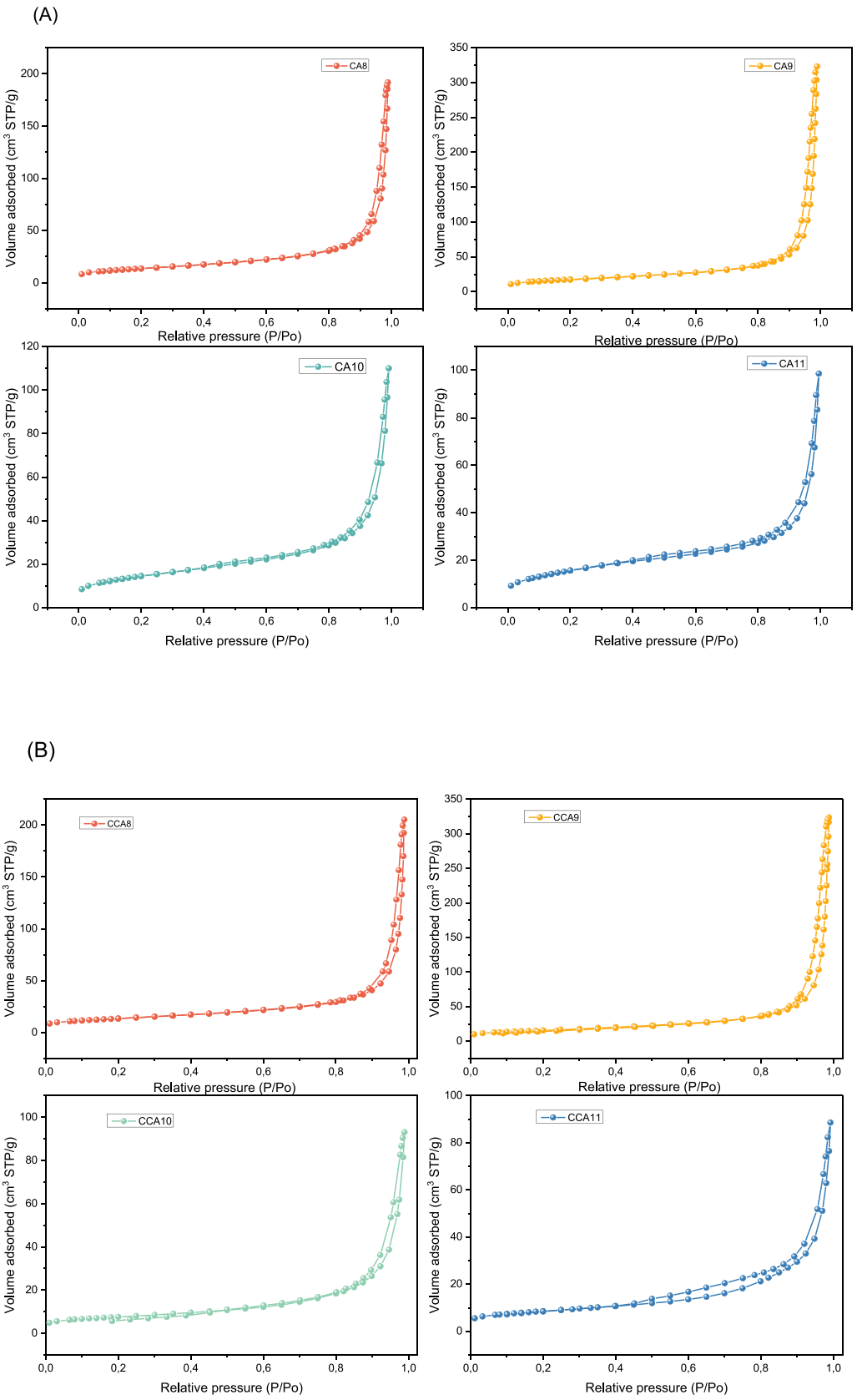

Fig. 6. N_2 adsorption/desorption measurements at −196 °C of **(A)** uncalcined and **(B)** calcined samples.

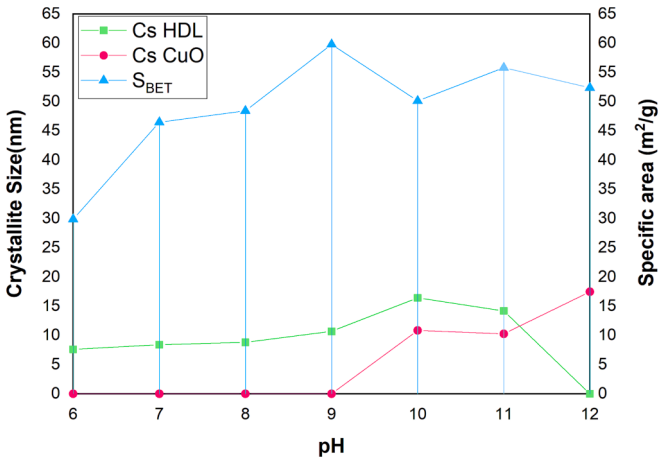

Fig. 7. Crystallite size (Cs) and BET specific surface area (S_{BET}) comparison. Crystallite size of CuAl LDH (green) and CuO (pink) as a function of pH determined by the Debye–Scherrer equation based on (200) and (111) XRD peaks, respectively. (For interpretation of the references to colour in this figure legend, the reader is referred to the web version of this article.)

3.3. H_2-Temperature programmed reduction

The TPR profiles of calcined CuAl LDH synthesized at various pH levels are shown in Fig. 9. The reduction profiles can be divided into: α, β and γ. The gradual reduction of copper oxide CuO (i.e. at low temperature Cu^{2+} changes to Cu^{+} and at high temperature Cu^{+} changes to metallic copper Cu^{0}) is not so easy to solve, as there are several mass fractions present in the samples which interact in different forms. They can be classified into α, α, β, γ and γ́ (multi-peaks adjusted according to the Gaussian method) and could remain linked to the structural and/or morphological differences of the entities of copper oxide involved. The first, noted (α) and located at lower temperature, is attributed to the reduction of highly dispersed copper oxide species on the surface. The peak noted (β) is attributed to species of larger and well dispersed CuO clusters (cluster). The peak located at a higher temperature (γ) is attributed to larger particles of crystalline CuO type (bulk) (Dib et al., 2020; Bridier et al., 2010; Dow et al., 2000; Cecilia et al., 2017). It can be seen that the latter (γ) moves towards lower temperatures with the increase in the pH rate from 327–319–300–298 °C for pH = 8-9-10-11, respectively (see Fig. 9-**A**).

For CCA8 the appearance of two peaks in the α region with temperatures T_{max} of reduction 238–275 °C (for α, α, respectively) and another peak (β) at 293 °C (see Fig. 9-**B** and Table 4) could be associated with different morphology, size and total mass distribution, of copper oxide in the sample as well as unwanted impurities or secondary phases during synthesis. On this curve, the largest mass fraction with 43% for the peak (γ) presents the strongest interaction for a temperature T_{max} of 327 °C, perhaps probably due to the reduction of the particles in the larger copper oxide agglomerate (CuO/cristaline CuO) leading to low dispersion metallic copper. In the case of CCA9, the distribution of the mass fraction changes increasing its percentage towards a smaller

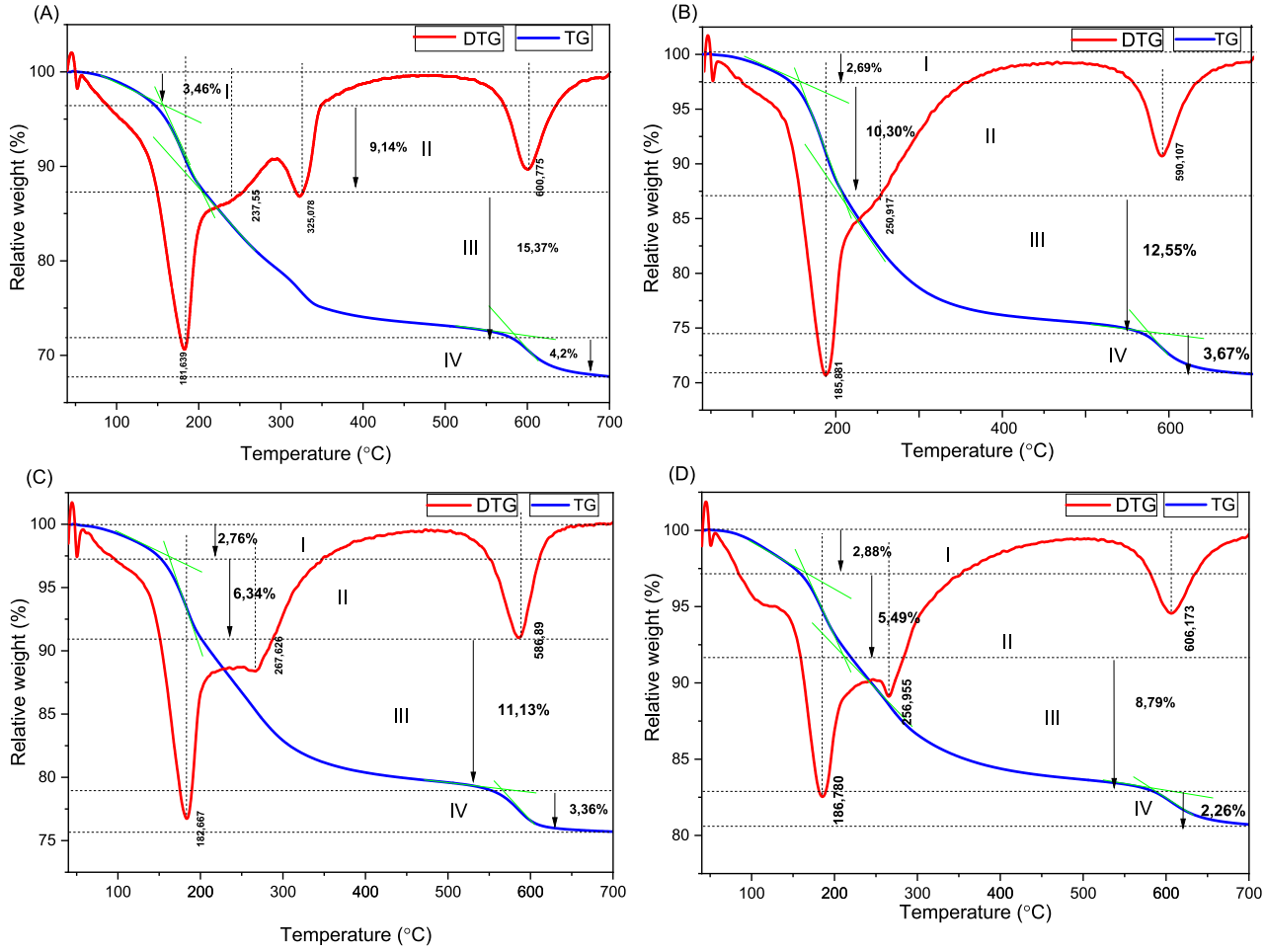

Fig. 8. TGA – DTG profiles of CuAl LDH synthesized at various pH. **(A)** CA8, **(B)** CA9, **(C)** CA10, **(D)** CA11 samples at pH = 8, 9, 10, 11, respectively. The samples where heated at rate of 20 °C/min in N_2 atmosphere (50 mL/min).

Table 3
Thermogravimetric parameters of the synthesized samples.

Temperature Samples	I 40–160 °C	II 160–210 °C	III 210–570 °C	IV 570–700 °C	**Total weight loss (%)**
CA8	3.46%	9.14%	15.37 %	4.2%	32.17
CA9	2.69%	10.30 %	12.55%	3.67%	29.21
CA10	2.76%	6.34 %	11.13 %	3.36%	23.59
CA11	2.88%	5.49%	8.79%	2.26%	19.42

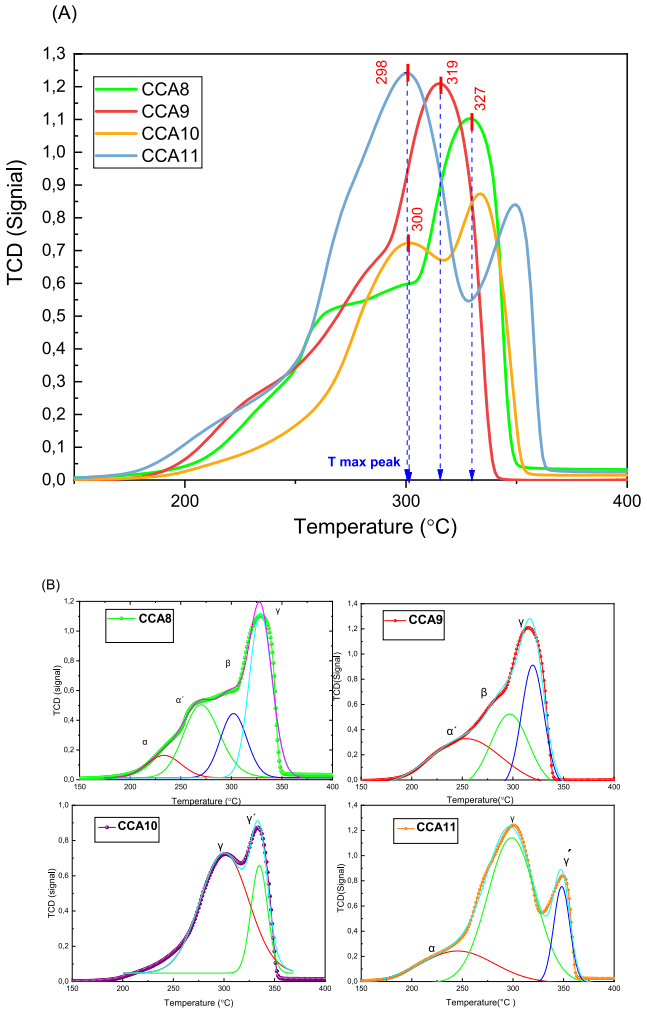

Fig. 9. (A) TPR patterns of the CuAl LDH calcined at 400 °C (LDO). **(B)** Peak deconvolution for CCA8 (pH = 8), CCA9 (pH = 9), CCA10 (pH = 10), CCA11 (pH = 11).

Table 4
Reducibility degree obtained from H_2-TPR profiles for CCA8-CCA9-CCA10 and CCA11 samples synthesized at several pH levels.

Peak	Area (%)	Temperature (°C)	Peak	Area (%)	Temperature (°C)
CCA8			**CCA9**		
α	12.01	248	**α′**	39.34	255
α′	21.9	261	**β**	31.3	297
β	24.02	293	**γ**	29.34	319
γ	43.05	327			
CCA10			**CCA11**		
γ	74.89	300	**α**	20.59	243
γ′	25.1	334	**γ**	62.15	298
			γ′	17.26	348

reduction temperature thus showing a greater distribution of copper oxide and explaining the increase in the specific surface area. With the existence of reduction steps at fairly close temperatures, we are talking about a similar interaction of species having the same morphology and/or different size. It can be said that the increase in the concentration of hydroxides will generate the formation of structural species of Cu less anchored to the surface, generating a decrease at lower temperature. In other words, a lower reduction temperature indicates a lower stability of these Cu phases. In the CCA9X sample, a significant observation lies in the emergence of three distinct peaks, localized respectively within the domains corresponding to the α, αand β (see **Table S2**). In comparison with CCA9, a shift towards lower temperatures is observed. Simultaneously, it is noted that the mass fraction consistently remains concentrated on the ά̀peak as displayed in in **Fig. S5.** The mass fraction of the reduced bulk copper oxide species corresponding to the region (γ) for the CCA10 sample is 74% (T_{max} of 300 °C) with the disappearance of the smallest interaction peaks (corresponding to α and α'). 62% of the total mass is reduced at the same temperature range (298 °C) in CCA11 and in both samples another peak (γ́) appears at larger T_{max} (334 and 348 °C for CCA10 and CCA11, respectively). The formation of the latter is reported as the peak obtained from Cu_2O as an intermediate in reduction processes in samples with a high copper content (Teixeira et al., 2018; Dumas et al., 1989). Thus, the γ and γ́ peaks are explained by the reduction of CuO on the surface according to the reaction: 2 CuO + H_2 → Cu_2O + H_2O and the next step is from Cu_2O + H_2 → Cu + H_2O. The emergence of Cu^+ generates higher reduction temperatures at higher copper content. Due to its existence in a stable way in the oxygen vacancy defects from where CuO would operate for the formation of Cu_2O, possibly copper reduced at high temperatures may well react with copper oxide to form the latter according to the following reaction: Cu + CuO → Cu_2O (Dumas et al., 1989). At a high copper content, the proportion of bulk particles increases, which implies a transition from smaller CuO particles to larger particles, thus disfavoring the distribution of Cu^{2+} in the surface. Furthermore, the type of copper species present in the samples contributes significantly to the change in reducibility.

4. Conclusions

The synthesis of a phase-pure CuAl LDH with a molar ratio of 3:1 and aluminum salt slag residues as a source of aluminum by a simple technique of co-precipitation is for the first time demonstrated. As the chemistry of LDH is versatile and sensitive to the preparation conditions, different parameters must be considered. The characteristics of the hydrotalcite as well as its oxide have been demonstrated to depend on the pH, the aging time and the calcination temperature. From our experimental studies, it is concluded that the pH has a significant effect on the formation of hydrotalcites and that by its influence on the precipitation of cations, the content of precipitated copper becomes greater as the pH increases. At a more alkaline pH, i.e. 12, the hydrotalcite phase is not favored but rather the formation of a predominant crystalline phase of CuO. It has also been demonstrated that the change in pH directly affects the amount and type of structure obtained, the enrichment and the nature of the secondary phases, as well as the morphological and structural properties of the synthesized samples. The increase in the concentration of OH^- ions does not only affect the

dispersion of copper (it has also been found that the proportion of loose particles increases with a high copper content) but also affects the reducibility of this metal by favoring its reduction at lower temperatures. Although the calcination at 400 °C of the CuAl hydrotalcite generates sintering, the nanoplatelet-like morphology was preserved, the latter was not destroyed while observing spherical agglomerates of copper nanoparticles developing on the LDH structures. The higher increase of the calcination temperature leads to the formation of $CuAl_2O_4$ and $CuAl_2$ spinel with a higher crystallinity rate for copper oxide thus showing a total destruction of LDH.

CRediT authorship contribution statement

A.I. Boulahbal: Conceptualization, Methodology, Writing – original draft, Investigation. **L. Santamaría:** Methodology, Writing – original draft, Investigation, Writing – review & editing. **A. Azizi:** Conceptualization, Writing – review & editing. **M. Boutahala:** Conceptualization, Writing – review & editing. **S.A. Korili:** Supervision, Writing – review & editing. **A. Gil:** Conceptualization, Methodology, Writing – original draft, Supervision, Writing – review & editing.

Declaration of Competing Interest

The authors declare that they have no known competing financial interests or personal relationships that could have appeared to influence the work reported in this paper.

Data availability

No data was used for the research described in the article.

Acknowledgements

The authors are grateful for financial support from the Spanish Ministry of Science and Innovation (MCIN/AEI/10.13039/501100011033) through project PID2020-112656RB-C21. Open access funding provided by Universidad Pública de Navarra for a post-doctoral Margarita Salas grant, financed by the European Union-Next Generation EU.

Appendix A. Supplementary material

Supplementary data to this article can be found online at https://doi.org/10.1016/j.mineng.2023.108413.

References

Aflak, N., el Mersly, L., ben EL Ayouchia, H., Rafqah, S., Anane, H., Julve, M., Stiriba, S. E., 2022. A new Cu3Al-layered double hydroxide heterogeneous catalyst for azide-alkyne [3 + 2] cycloaddition reaction in water. J. Coord. Chem. 75, 2346–2358. https://doi.org/10.1080/00958972.2022.2105701.

Angelescu, E., Pavel, O.D., Bîrjega, R., Florea, M., Zăvoianu, R., 2008. The impact of the "memory effect" on the catalytic activity of Mg/Al; Mg, Zn/Al; Mg/Al, Ga hydrotalcite-like compounds used as catalysts for cycloxene epoxidation. Appl. Catal. A Gen. 341, 50–57. https://doi.org/10.1016/j.apcata.2007.12.022.

Arabi, M., Ghaedi, M., Ostovan, A., Tashkhourian, J., Asadallahzadeh, H., 2016. Synthesis and application of molecularly imprinted nanoparticles combined ultrasonic assisted for highly selective solid phase extraction trace amount of celecoxib from human plasma samples using design expert (DXB) software. Ultrason. Sonochem. 33, 67–76. https://doi.org/10.1016/j.ultsonch.2016.04.022.

Asfaram, A., Ghaedi, M., Dashtian, K., 2017. Rapid ultrasound-assisted magnetic microextraction of gallic acid from urine, plasma and water samples by HKUST-1-MOF-Fe_3O_4-GA-MIP-NPs: UV–vis detection and optimization study. Ultrason. Sonochem. 34, 561–570. https://doi.org/10.1016/j.ultsonch.2016.06.033.

Bart, J.C.J., Sneeden, R.P.A., 1987. Copper-zinc oxide-alumina methanol catalysts revisited. Catal. Today 2, 1–124. https://doi.org/10.1016/0920-5861(87)80001-9.

Berner, S., Araya, P., Govan, J., Palza, H., 2018. Cu/Al and Cu/Cr based layered double hydroxide nanoparticles as adsorption materials for water treatment. J. Ind. Eng. Chem. 59, 134–140. https://doi.org/10.1016/j.jiec.2017.10.016.

Boclair, J.W., Braterman, P.S., 1999. Layered double hydroxide stability. 1. Relative stabilities of layered double hydroxides and their simple counterparts. Chem. Mater. 11, 298–302. https://doi.org/10.1021/cm980523u.

Bridier, B., López, N., Pérez-Ramírez, J., 2010. Partial hydrogenation of propyne over copper-based catalysts and comparison with nickel-based analogues. J. Catal. 269, 80–92. https://doi.org/10.1016/j.jcat.2009.10.019.

Britto, S., Vishnu Kamath, P., 2009. Thermal, solution and reductive decomposition of Cu–Al layered double hydroxides into oxide products. J. Solid State Chem. 182, 1193–1199. https://doi.org/10.1016/j.jssc.2009.02.003.

Brunauer, S., Deming, L.S., Deming, W.E., Teller, E., 1940. On a theory of the van der waals adsorption of gases. J. Am. Chem. Soc. 62, 1723–1732. https://doi.org/10.1021/ja01864a025.

Bukhtiyarova, M.V., 2019. A review on effect of synthesis conditions on the formation of layered double hydroxides. J Solid State Chem. 269, 494–506. https://doi.org/10.1016/j.jssc.2018.10.018.

Busetto, C., del Piero, G., Manara, G., Trifirò, F., Vaccari, A., 1984. Catalysts for low-temperature methanol synthesis. Preparation of Cu□Zn□Al mixed oxides via hydrotalcite-like precursors. J. Catal. 85, 260–266. https://doi.org/10.1016/0021-9517(84)90130-1.

Cardona, Y., Korili, S.A., Gil, A., 2021. A nonconventional aluminum source in the production of alumina-pillared clays for the removal of organic pollutants by adsorption. Chem. Eng. J. 425, 130708 https://doi.org/10.1016/j.cej.2021.130708.

Cecilia, J.A., Arango-Díaz, A., Marrero-Jerez, J., Núñez, P., Moretti, E., Storaro, L., Rodríguez-Castellón, E., 2017. Catalytic behaviour of CuO-CeO_2 systems prepared by different synthetic methodologies in the CO-PROX reaction under CO_2-H_2O feed stream. Catalysts 7, 1–20. https://doi.org/10.3390/catal7050160.

Cudennec, Y., Lecerf, A., 2001. Étude du type structural de γ-FeO(OH)(s) et comparaison avec la structure de Cu(OH)2(s). C. R. Chim. 4, 885–891. https://doi.org/10.1016/s1387-1609(01)01303-2.

Dib, H., el Khawaja, R., Rochard, G., Poupin, C., Siffert, S., Cousin, R., 2020. Cualce oxides issued from layered double hydroxide precursors for ethanol and toluene total oxidation. Catalysts 10, 1–14. https://doi.org/10.3390/catal10080870.

Dinari, M., Soltani, R., Mohammadnezhad, G., 2017. Kinetics and Thermodynamic Study on Novel Modified-Mesoporous Silica MCM-41/Polymer Matrix Nanocomposites: Effective Adsorbents for Trace CrVI Removal. J. Chem. Eng. Data. 62, 2316–2329. https://doi.org/10.1021/acs.jced.7b00197.

Dow, W.-P., Wang, Y.-P., Huang, T.-J., 2000. TPR and XRD studies of yttria-doped ceria/γ-alumina-supported copper oxide catalyst. Appl. Catal. A Gen. 190, 25–34. https://doi.org/10.1016/S0926-860X(99)00286-0.

Dumas, J.M., Geron, C., Kribii, A., Barbier, J., 1989. Preparation of supported copper catalysts. II. Reduction of copper/alumina catalysts. Appl. Catal. 47, L9–L15. https://doi.org/10.1016/S0166-9834(00)83256-X.

Fan, G., Li, F., Evans, D.G., Duan, X., 2014. Catalytic applications of layered double hydroxides: Recent advances and perspectives. Chem. Soc. Rev. 43, 7040–7066. https://doi.org/10.1039/c4cs00160e.

Fornari, A.C., Neto, R.M., Lenzi, G.G., Santos, O.A.A., Jorge, L.M.M., 2017. Utilization of sol-gel CuO-ZnO-Al2O3 catalysts in the methanol steam reforming for hydrogen production. Can. J. Chem. Eng. 95, 2258–2271. https://doi.org/10.1002/cjce.23005.

Gao, Q., Guo, Q., Li, Y., Ren, B., Fu, M., Li, H., Tian, D., Ding, M., 2021. Innovative technology for defluorination of secondary aluminum dross by alkali leaching. Miner. Eng. 172, 107134 https://doi.org/10.1016/j.mineng.2021.107134.

Gil, A., 2005. Management of the salt cake from secondary aluminum fusion processes. Ind. Eng. Chem. Res. 44, 8852–8857. https://doi.org/10.1021/ie050835o.

Gil, A., Korili, S.A., 2016. Management and valorization of aluminum saline slags: Current status and future trends. Chem. Eng. J. 289, 74–84. https://doi.org/10.1016/j.cej.2015.12.069.

Gil, A., Albeniz, S., Korili, S.A., 2014. Valorization of the saline slags generated during secondary aluminium melting processes as adsorbents for the removal of heavy metal ions from aqueous solutions. Chem. Eng. J. 251, 43–50. https://doi.org/10.1016/j.cej.2014.04.056.

Gil, A., Arrieta, E., Vicente, M.A., Korili, S.A., 2018. Synthesis and CO_2 adsorption properties of hydrotalcite-like compounds prepared from aluminum saline slag wastes. Chem. Eng. J. 334, 1341–1350. https://doi.org/10.1016/j.cej.2017.11.100.

Guan, X., Yuan, X., Zhao, Y., Wang, H., Wang, H., Bai, J., Li, Y., 2022. Application of functionalized layered double hydroxides for heavy metal removal: A review. Sci. Total Environ. 838, 155693 https://doi.org/10.1016/j.scitotenv.2022.155693.

Guo, X., Zhang, F., Peng, Q., Xu, S., Lei, X., Evans, D.G., Duan, X., 2011. Layered double hydroxide/eggshell membrane: An inorganic biocomposite membrane as an efficient adsorbent for Cr(VI) removal. Chem. Eng. J. 166, 81–87. https://doi.org/10.1016/j.cej.2010.10.010.

Haraketi, M., Hosni, K., Srasra, E., 2017. Intercalation behavior of salicylic acid into calcined Cu-Al-layered double hydroxides for a controlled release formulation. Surf. Eng. Appl. Electrochem. 53, 360–370. https://doi.org/10.3103/S106837551704007X.

High, M., Patzschke, C.F., Zheng, L., Zeng, D., Gavalda-Diaz, O., Ding, N., Chien, K.H.H., Zhang, Z., Wilson, G.E., Berenov, A.V., Skinner, S.J., Sedransk Campbell, K.L., Xiao, R., Fennell, P.S., Song, Q., 2022. Precursor engineering of hydrotalcite-derived redox sorbents for reversible and stable thermochemical oxygen storage. Nat. Commun. 13, 5109. https://doi.org/10.1038/s41467-022-32593-6.

Hubbell, J.A., Chilkoti, A., 2012. Nanomaterials for drug delivery. Science 337, 303–305. https://doi.org/10.1126/science.1219657.

Intissar, M., Seron, A., Giovannelli, F., Autret, C., Motelica-Heino, M., Delorme, F., 2015. Effect of copper content on the synthesis and properties of (Mg4−xCux) Al2OH12CO3, nH2O layered double hydroxides. J. Mater. Sci. 50, 1427–1434. https://doi.org/10.1007/s10853-014-8702-5.

Kannan, S., 2006. Catalytic applications of hydrotalcite-like materials and their derived forms. Catal. Surv. Asia 10, 117–137. https://doi.org/10.1007/s10563-006-9012-y.

Kannan, S., Rives, V., Knözinger, H., 2004. High-temperature transformations of Cu-rich hydrotalcites. J. Solid State Chem. 177, 319–331. https://doi.org/10.1016/j.jssc.2003.08.023.

Kühl, S., Friedrich, M., Armbrüster, M., Behrens, M., 2012. Cu, Zn, Al layered double hydroxides as precursors for copper catalysts in methanol steam reforming - PH-controlled synthesis by microemulsion technique. J. Mater. Chem. 22, 9632–9638. https://doi.org/10.1039/c2jm16138a.

Li, D., Cai, Y., Ding, Y., Li, R., Lu, M., Jiang, L., 2015. Layered double hydroxides as precursors of Cu catalysts for hydrogen production by water-gas shift reaction. Int. J Hydrogen Energy. 40, 10016–10025. https://doi.org/10.1016/j.ijhydene.2015.05.183.

Li, M.M.J., Chen, C., Ayvall, T., Suo, H., Zheng, J., Teixeira, I.F., Ye, L., Zou, H., O'Hare, D., Tsang, S.C.E., 2018. CO_2 Hydrogenation to Methanol over Catalysts Derived from Single Cationic Layer CuZnGa LDH Precursors. ACS Catal. 8, 4390–4401. https://doi.org/10.1021/acscatal.8b00474.

Lu, Z., Qian, L., Tian, Y., Li, Y., Sun, X., Duan, X., 2016. Ternary NiFeMn layered double hydroxides as highly-efficient oxygen evolution catalysts. Chem. Commun. 52, 908–911. https://doi.org/10.1039/c5cc08845c.

Lwin, Y., Yarmo, M.A., Yaakob, Z., Mohamad, A.B., Daud, W.R.W., 2001. Synthesis and characterization of Cu-Al layered double hydroxides. Mater. Res. Bull. 36, 193–198. https://doi.org/10.1016/S0025-5408(01)00491-3.

Mahinroosta, M., Allahverdi, A., 2018. Hazardous aluminum dross characterization and recycling strategies: A critical review. J. Environ. Manage. 223, 452–468. https://doi.org/10.1016/j.jenvman.2018.06.068.

Mohammadnezhad, G., Dinari, M., Soltani, R., Bozorgmehr, Z., 2015. Thermal and mechanical properties of novel nanocomposites from modified ordered mesoporous carbon FDU-15 and poly(methyl methacrylate). Appl. Surf. Sci. 346, 182–188. https://doi.org/10.1016/j.apsusc.2015.04.005.

Montanari, B., Vaccari, A., Gazzano, M., Käßner, P., Papp, H., Pasel, J., Dziembaj, R., Makowski, W., Lojewski, T., 1997. Characterization and activity of novel copper-containing catalysts for selective catalytic reduction of NO with NH_3. Appl. Catal. B Environ. 13, 205–217. https://doi.org/10.1016/S0926-3373(96)00106-3.

Nagendra, B., Mohan, K., Bhoje Gowd, E., 2015. Polypropylene/Layered Double Hydroxide (LDH) Nanocomposites: Influence of LDH Particle Size on the Crystallization Behavior of Polypropylene. ACS Appl. Mater. Interfaces 7, 12399–12410. https://doi.org/10.1021/am5075826.

Nejati, K., Akbari, A.R., Davari, S., Asadpour-Zeynali, K., Rezvani, Z., 2018. Zn-Fe-layered double hydroxide intercalated with vanadate and molybdate anions for electrocatalytic water oxidation. New J. Chem. 42, 2889–2895. https://doi.org/10.1039/c7nj04469k.

Obalová, L., Karásková, K., Jirátová, K., Kovanda, F., 2009. Effect of potassium in calcined Co-Mn-Al layered double hydroxide on the catalytic decomposition of N_2O. Appl. Catal. B Environ. 90, 132–140. https://doi.org/10.1016/j.apcatb.2009.03.002.

Palapa, N.R., Juleanti, N., Normah, R., Mohadi, T., Taher, A., Rachmat, A.L., 2020. Copper aluminum layered double hydroxide modified by biochar and its application as an adsorbent for procion red. J. Water Environ. Technol. 18, 359–371. https://doi.org/10.2965/JWET.20-059.

Santamaría, L., Vicente, M.A., Korili, S.A., Gil, A., 2020. Saline slag waste as an aluminum source for the synthesis of Zn–Al–Fe–Ti layered double-hydroxides as catalysts for the photodegradation of emerging contaminants. J Alloys Compd. 843, 156007 https://doi.org/10.1016/j.jallcom.2020.156007.

Santamaría, L., Korili, S.A., Gil, A., 2022. Layered double hydroxides from slags: Closing the loop. J. Environ. Chem. Eng. 10 https://doi.org/10.1016/j.jece.2021.106948.

Sanvicens, N., Marco, M.P., 2008. Multifunctional nanoparticles - properties and prospects for their use in human medicine. Trends Biotechnol. 26, 425–433. https://doi.org/10.1016/j.tibtech.2008.04.005.

Segal, S.R., Carrado, K.A., Marshall, C.L., Anderson, K.B., 2003. Catalytic decomposition of alcohols, including ethanol, for in situ H_2 generation in a fuel stream using a layered double hydroxide-derived catalyst. Appl. Catal. A Gen. 248, 33–45. https://doi.org/10.1016/S0926-860X(03)00132-7.

Sertsova, A.A., Subcheva, E.N., E. v Yurtov, 2015. Synthesis and study of structure formation of layered double hydroxides based on Mg, Zn, Cu, and Al, Russian. J. Inorg. Chem. 60, 23–32. https://doi.org/10.1134/S0036023615010167.

Shannon, I.J., Rey, F., Sankar, G., Thomas, J.M., Maschmeyer, T., Waller, A.M., Palomares, A.E., Corma, A., Dent, A.J., Greaves, G.N., 1996. Hydrotalcite-derived mixed oxides containing copper: catalysts for the removal of nitric oxide. J. Chem. Soc., Faraday Trans. 92, 4331–4336. https://doi.org/10.1039/FT9969204331.

Song, Q., Liu, W., Bohn, C.D., Harper, R.N., Sivaniah, E., Scott, S.A., Dennis, J.S., 2013. A high performance oxygen storage material for chemical looping processes with CO_2 capture. Energy Environ. Sci. 6, 288–298. https://doi.org/10.1039/c2ee22801g.

Teixeira, C.D.O.P., Montani, S.D.S., Palacio, L.A., Zotin, F.M.Z., 2018. The effect of preparation methods on the thermal and chemical reducibility of Cu in Cu-Al oxides. Dalton Transactions. 47, 10989–11001. https://doi.org/10.1039/c8dt01150h.

Tenorio, J.A.S., Espinosa, D.C.R., 2002. Effect of salt/oxide interaction on the process of aluminum recycling. J. Light Met. 2, 89–93. https://doi.org/10.1016/S1471-5317(02)00027-5.

Tien Thao, N., Kim Huyen, L.T., 2015. Catalytic oxidation of styrene over Cu-doped hydrotalcites. Chem. Eng. J. 279, 840–850. https://doi.org/10.1016/j.cej.2015.05.090.

Torrez-Herrera, J.J., Korili, S.A., Gil, A., 2022. Bimetallic (Pt-Ni) La-hexaaluminate catalysts obtained from aluminum saline slags for the dry reforming of methane. Chem. Eng. J. 433, 133191 https://doi.org/10.1016/j.cej.2021.133191.

Valente, J.S., Figueras, F., Gravelle, M., Kumbhar, P., Lopez, J., Besse, J.P., 2000. Basic properties of the mixed oxides obtained by thermal decomposition of hydrotalcites containing different metallic compositions. J. Catal. 189, 370–381. https://doi.org/10.1006/jcat.1999.2706.

van Everbroeck, T., Wu, J., Arenas-Esteban, D., Ciocarlan, R.G., Mertens, M., Bals, S., Dujardin, C., Granger, P., Seftel, E.M., Cool, P., 2022. ZnAl layered double hydroxide based catalysts (with Cu, Mn, Ti) used as noble metal-free three-way catalysts. Appl. Clay Sci. 217, 106390 https://doi.org/10.1016/j.clay.2021.106390.

Velu, S., Swamy, C.S., 1996. Selective C-alkylation of phenol with methanol over catalysts derived from copper-aluminium hydrotalcite-like compounds. Appl. Catal. A Gen. 145, 141–153. https://doi.org/10.1016/0926-860X(96)00133-0.

Verma, S.K., Dwivedi, V.K., Dwivedi, S.P., 2020. Utilization of aluminium dross for the development of valuable product - A review. Mater. Today Proc. 43, 547–550. https://doi.org/10.1016/j.matpr.2020.12.045.

Voyer, N., Soisnard, A., Palmer, S.J., Martens, W.N., Frost, R.L., 2009. Thermal decomposition of the layered double hydroxides of formula Cu6Al2(OH)16CO3 and Zn6Al2(OH)16CO3. J. Therm. Anal. Calorim. 96, 481–485. https://doi.org/10.1007/s10973-008-9169-x.

Xia, S., Zhang, L., Zhou, X., Pan, G., Ni, Z., 2015. The photocatalytic property for water splitting and the structural stability of CuMgM layered double hydroxides (M=Al, Cr, Fe, Ce). Appl. Clay Sci. 114, 577–585. https://doi.org/10.1016/j.clay.2015.06.023.

Yadav, D.K., Uma, S., Nagarajan, R., 2022. Microwave-assisted synthesis of ternary Li-M-Al LDHs (M = Mg Co, Ni, Cu, Zn, and Cd) and examining their use in phenol oxidation. Appl. Clay Sci. 228, 106655 https://doi.org/10.1016/j.clay.2022.106655.

Yamaoka, T., Abe, M., Tsuji, M., 1989. Synthesis of Cu-Al hydrotalcite like compound and its ion exchange property. Mater. Res. Bull. 24, 1183–1199. https://doi.org/10.1016/0025-5408(89)90193-1.

Yoldi, M., Fuentes-Ordoñez, E.G., Korili, S.A., Gil, A., 2020. Zeolite synthesis from aluminum saline slag waste. Powder Technol. 366, 175–184. https://doi.org/10.1016/j.powtec.2020.02.069.

Zhang, M., Yao, Q., Lu, C., Li, Z., Wang, W., 2014. Layered double hydroxide-carbon dot composite: High-performance adsorbent for removal of anionic organic dye. ACS Appl. Mater. Interfaces 6, 20225–20233. https://doi.org/10.1021/am505765e.